ESTIMATION AND TRACKING OF MAINTENANCE AND DAMAGE ON ADVANCED AIR MOBILITY CONCEPTS

Sheldon Salins, Georgia Institute of Technology, Atlanta, GA, USA
Aaron Crawford, Georgia Institute of Technology, Atlanta, GA, USA
Graeme J. Kennedy, Georgia Institute of Technology, Atlanta, GA, USA
Marilyn J. Smith, Georgia Institute of Technology, Atlanta, GA, USA

Abstract

Anticipated Advanced Air Mobility (AAM) operations for passenger travel and package delivery in urban and suburban environments introduces challenges for flight operations and the business models. The expected increase in flight cycles and increased vehicle-human interactions with passengers and maintenance personnel, can lead to a greater possibility of impact damage. Many of these vehicles will be constructed of advanced composites, such as exemplar thermoplastic material examined herein. The sensitivity of a thermoplastic demonstrator panel is analyzed for different integration boundary conditions, skin thicknesses, and how much information about the composite layup is known. In addition, the effect of impact damage and high frequency unsteady airloads, such as those encountered in rotor wakes, are examined. Details of the composite layout may not be required for assessment of damage, with appropriate safety factors. High vibratory airloads do influence the potential failure of composite panels, so that judicious selection rotor velocity may extend the life of panels. Damage depends on the location and skin thickness; skin damage near structural support members may be less problematic.

1. INTRODUCTION

The vertical lift community has been experiencing a resurgence in new design concepts and corresponding analysis software for civilian Advanced Air Mobility (AAM) operations (1). Advanced Air Mobility (AAM) vehicles will need to meet a fundamentally different set of requirements (2) than vehicles that perform traditional general aviation or rotorcraft missions. AAM must be able to perform, at much higher utilization, well within the atmospheric boundary layer across urban and suburban environments. Current planned operations tend to ground-based delivery and ride-share use cases so that their operational and lifecycle costs must support these business models (3).

Significant portions of AAM flight operations may occur in the atmospheric boundary layer (ABL), and in particular within the roughness sublayer of the atmospheric boundary layer (ABL) where strong gusts, vortex flows, and shear layers are present, as illustrated in Fig. 1. Flight through these complex unsteady environments will likely result in a much larger fraction of potentially significant dynamic and vibratory loads on the vehicle. Flight safety and ride quality will also be influenced in this transient environment. The impact to vehicle lifecycle, as well as the time to maintenance and need to repair damage can be influenced if significant portions of flights occur in these ABL regions.

The Georgia Institute of Technology (GIT), along with university partners at University of South Carolina (UofSC), North Carolina A & T (NCAT), and Middle Georgia State University (MGA), as well as corporate partner, Qarbon Aerospace, are addressing these concerns via a NASA University Leadership Initiative (ULI) project. The ULI project seeks improve AAM affordability and safety by developing simulation tools that track cost, safety, and performance of operational vehicles. In addition, it strives to develop approaches that will allow the aerospace community to transition new advanced materials for use in AAM vehicles.

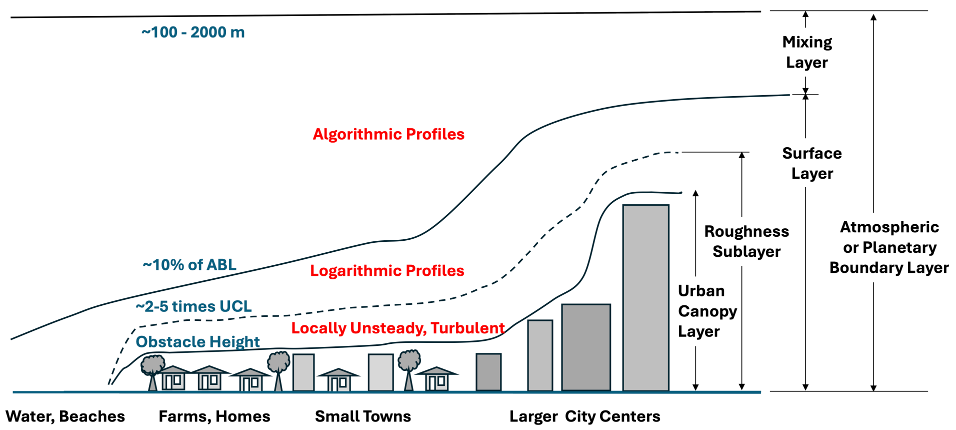

Figure 1: A representative schematic of the atmospheric boundary layer where AAM flights are planned, based on information in Refs. (4–6).

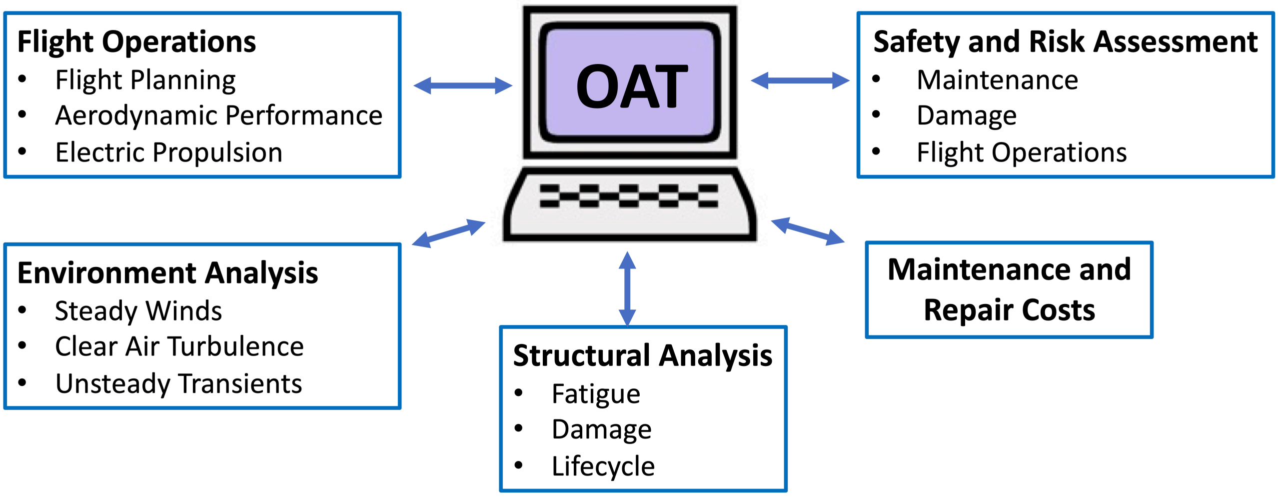

Figure 2: Operational Analysis Toolkit (OAT) components with modules. Courtesy Ref. (7).

A major objective of this ULI is the development of a software framework, the Operational Analysis Tool (OAT), that will allow operators to monitor flight conditions for safety, plan flights and operations, and assess individual vehicle structural health for maintenance and repair in near real time on personal computers (see Fig. 2). Each vehicle will be monitored in-flight via a suite of sensors, optimized for the vehicle configuration. The OAT will analyze these data post flight and provide status and recommendation for repair and maintenance of these vehicle structural components, as well as estimates on the remaining component lifecycle. These flight data are coupled with the real-time local flight environment and ABL to further enhance these estimates and improve safety. Another OAT use-case combines historical environmental data with statistical predictions to assess structural life, provide synthetic loads data for simulation of sensor systems, and estimate maintenance interval requirements based on the planned or actual flight routes.

The core of the OAT includes several component areas of analysis:

- Flight Planning and Operations Analysis
- Local Environment Effects
- Structural Analysis
- Maintenance and Repair Estimates
- Safety and Risk Assessment

An overview of the OAT framework was presented at the 2023 VFS Annual Forum (7). This paper focuses on the development of a portion of the structural analysis model, specifically on the validation, bounding and assessment of unsteady vibratory loading that different AAM vehicles may encounter.

Estimates of the maintenance and tracking the damage on an AAM vehicle are driven by highly individualistic multiple factors, such as composite material, panel location, transient operational environments, etc. Therefore, the approach applied in this effort examines the influence of both static and dynamic airloads on the structural behavior of a notional structural panel comprised of varying thicknesses of a thermoplastic composite material. Different boundary conditions of the panel are assessed to create behavior bounds. Representative airloads for different rotor downwash are also examined to provide a broader understanding of the impact of these new AAM applications.

2. COMPUTATIONAL METHODOLOGY

2.1. Structural Dynamics

The structural dynamics analysis has been performed with the Toolkit for the Analysis of Composite Structures (TACS) (8, 9). TACS is a parallel finite-element (FE) analysis code capable of adjoint-based analysis and gradient-based design optimization with large numbers of design variables. The TACS library includes higher-order shell elements based on the mixed-interpolation of tensorial components (MITC) formulation (10), appropriate for modeling the thin-walled structures in AAM. TACS applies scalable parallel finite-element analysis techniques with these elements to solve the structural governing equations. In addition to solving the governing equations, TACS includes the capability to evaluate several structural objective functions (8), including structural mass, compliance, material failure constraints, and buckling constraints, all of which are important in developing the OAT.

The Engineering Sketch Pad (ESP) (11) was utilized to generate a CAD-level geometry and the varying fidelity structural meshes applied in this effort. In addition, ESP permits the definition of the structural properties on the model. ESP's graphical user interface employs an open-source feature-based parametric solid modeler OpenCSM (12) to aid in rapid CAD development.

2.2. Fluid Dynamics

To assess the influence of the high frequency rotor downwash on the composite structure, particularly after damage, rotor operational information from a number of different AAM vehicles was examined, as identified in Table 1. Synthetic airloads were created to represent notional AAM rotor configurations listed in this table. Using normalized pressure coefficient results taken from prior rotor-fuselage interaction studies, such as Shenoy et al. (13). The frequency content and magnitude represents a forward flight conditions with an advance ratio of 0.15 and thrust coefficient of 0.0064 extracted near the location of the demonstrator panel, at the location in red illustrated in Fig. 3.

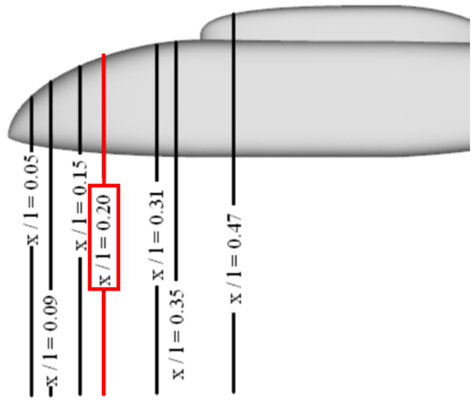

Figure 3: Airloads extraction location on the ROBIN fuselage. Modified figure from Shenoy et al. (13).

The data were then extrapolated to new combinations of rotor tip speed and number of blades. To correlate with AAM configurations, four notional scenarios were created to represent two rotor blade combinations (2 and 5) with low and high rotor tip speeds.

The magnitude of the synthetic loads is directly related to the square of the rotor tip speed. Figure 4 delineates the relative magnitude of the blade passing frequency content between the four scenarios. The data from the two-bladed highest tip speed provides the nondimensional basis for the different cases.

3. Panel Demonstrator Model

A full-scale 2.8 m radius curved panel, similar to what may be encountered on passenger-size AAM vehicles, was manufactured by the ULI partner, Qarbon Aerospace (18). The panel, details provided in Fig. 5 and Table 2, included four zones of varying skin thickness fabricated from Toray Cetex® TC1225 PAEK thermoplastic. The panel also included typical support structures, such as a keel beam and stringers.

The skin of the demonstrator was fabricated using automated fiber placement (AFP) technology, while the supporting structures were made by press forming, wherein preformed laminates are preheated to melt temperatures in an oven, then rapidly shuttled into a press and die to form the structural element. The press forming was aligned with the anticipated processing rates to be defined by AAM manufacturers.

The thickness of the skin panel decreases between four sections: 3.57 mm, 2.74 mm, 2.19 mm, and 1.37 mm. These regions are represented in Figure 6, where darker blue panel sections represent greater skin thickness. All structural frame elements have a

Table 1: Table of Different Vehicles Rotors in Cruise.

Vehicle Name	Designation	Number of Blades	Approximate RPM	Rotor Radius
Sikorsky UH-60 (14)	Helicopter	4	250 rpm	8.19 m
Boeing CH-47(14)	Helicopter	3	225 rpm	9.14 m
Bell AH-1 (14)	Helicopter	2	294-324 rpm	6.70 m
Airbus H125 (14)	Helicopter	3	400 rpm	5.22 m
Joby Aviation (15)	AAM	5	750 rpm	1.74 m (Estimated)
NASA Tilt Wing (16)	AAM	5	1400 rpm	1.11 m
NASA Lift + Cruise (1)	AAM	2	1100 - 1260 rpm	1.52 m
NASA Quadrotor (1)	AAM	3 or 5	570 rpm	2.80 m
SUI Endurance (17)	Drone	2	2500 - 4500 rpm	0.19 m
DJI Phantom 3 (17)	Drone	2	7500 rpm	0.12 m

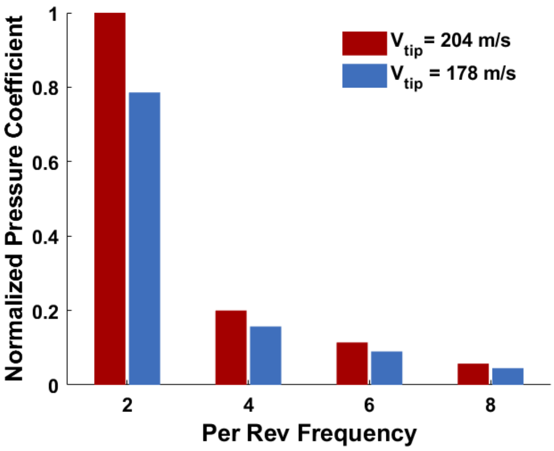

(a) Two Bladed Rotor

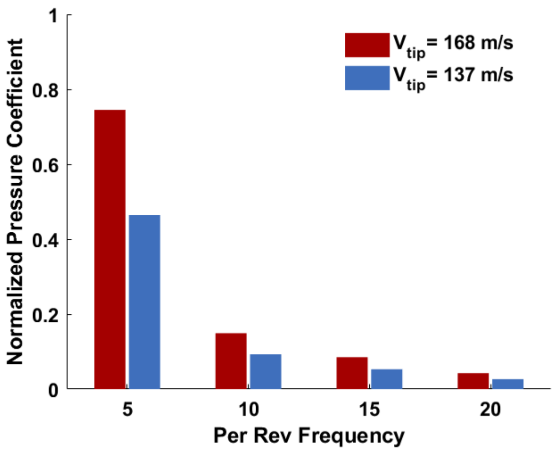

(b) Five Bladed Rotor

Figure 4: Normalized rotor tip speed for two and five bladed rotors as a function of the N-per-rev blade passing frequency.

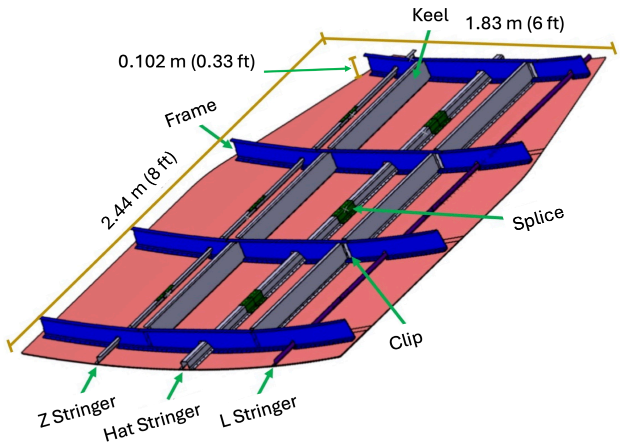

Figure 5: Demonstrator details, as fabricated by ULI partner Qarbon Aerospace (18).

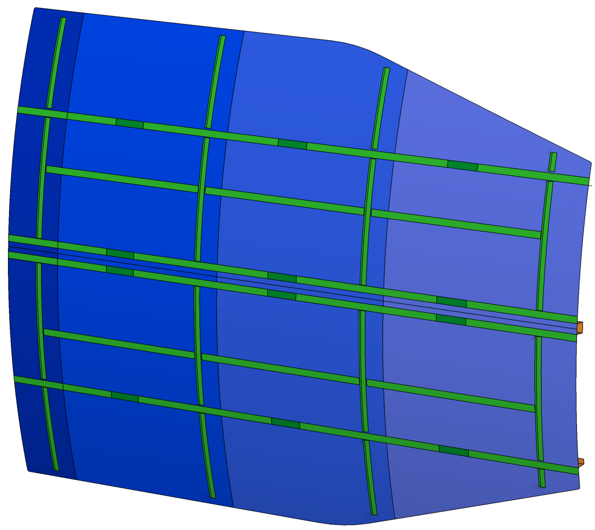

Figure 6: Demonstrator panel model in ESP, where darker blue regions are zones of greater laminate thickness and green regions define the thickness of overlapping frame elements and skin.

laminate thickness of 1.23 mm. Regions where frame or skin surfaces overlapped had a total thickness set to the sum of the overlapping components.

Table 2: Demonstrator Fabrication Details, Manufactured by ULI Partner Qarbon Aerospace (18).

Part	Dimension cm (in)	Manufacturing Method
Skin	247.1 × 177.8 × 7.6 (96 × 70 × 3)	AFP
Frames	177.8 × 20.3 × 2.5 (70 × 8 × 1)	AFP
Keel Beams	71.1 × 10.2 × 2.5 (28 × 4 × 1)	Press
Stringer	50.8 × 10.2 × 8.9 (20 × 4 × 3.5)	
Splice	50.8 × 11.4 × 4.1 (5 × 4.5 × 1.6)	Press

4. Validation and Computational Convergence

After fabrication, the demonstrator was subjected to static tests at the University of South Carolina (UofSC), another ULI partner. Two compressive loads of 355.9 N (80 lbs) and 667.2 N (150 lbs) were applied at the top of the panel, as illustrated in the lower right corner with the red I-beam element in Fig. 7. The deformations resulting from these tests were used to validate the numerical analysis.

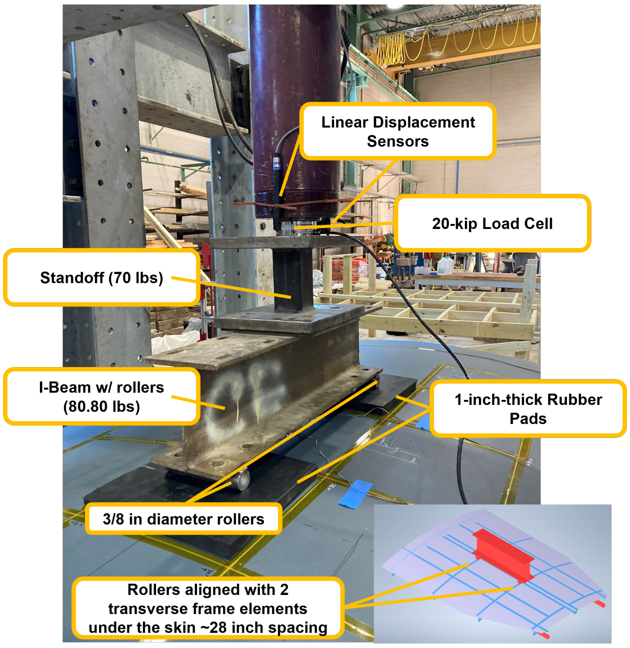

Figure 7: Static compression test rig with demonstrator panel setup. Tests performed at and by the University of South Carolina, Aerospace Engineering program, who are ULI partners. Photo courtesy of UoSC.

The convergence studies evaluated the Kreisselmeier-Steinhauser (19) failure index or value. The K-S failure value is defined as

$$\text{K-S}(g,\rho) = m + \frac{1}{\rho} ln\Big[\frac{1}{\alpha}\int_{\Omega} e^{\rho(g-m)} d\Omega\Big] \quad (1)$$

where α is a normalization factor, m is an arbitrary constant with a value of 10, Ω is the compact domain, g is a constrained function, ρ is an aggregation parameter. More detailed information about the use of the K-S index in the TACS software is found in Ref. (20). The effort reported on in this paper focused on the skin behavior, though the structural support elements were also modeled in these analyses. The validation of the methodology was performed by comparing with data obtained at the hardware skin strain gauge sensor locations, denoted by G-X1, G-X2, G-Y1, G-Y2, and G-Y3 in Fig. 8. Additional virtual "S" sensors, also shown in Fig. 8, were added throughout the panel to track convergence, as well as the panel behavior presented in the following sections.

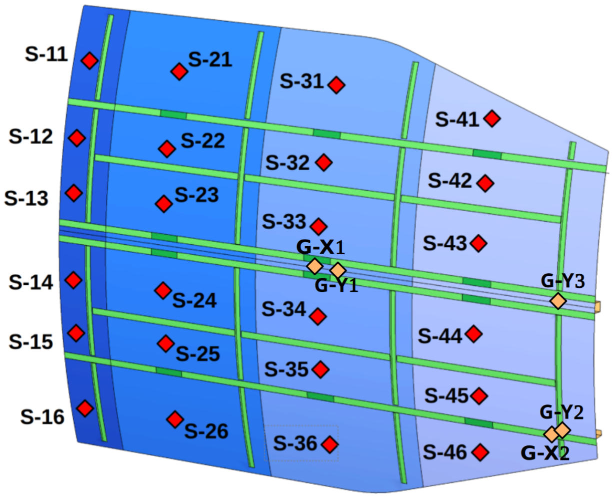

Figure 8: Demonstrator panel virtual skin probe array.

4.1. Mesh Convergence

The structural mesh convergence study considered the displacements of the structure as the convergence variable. Previous studies indicate that displacements from the TACS solver generally exhibit a clear asymptotic convergence trend with mesh size (8).

The mesh is generated by TACS at runtime. The global mesh settings define triangular surface elements, allowing a range of 3 to 50 points per edge, and a maximum dihedral angle of 5°. The global mesh size parameter is a sizing factor, which was varied from 0.1000 (coarsest) to 0.0050 (finest). The convergence criterion was a change less than 2% error, calculated using the finest mesh resolution results as the true value. A representative subset of the probe points displayed in Fig. 8 was selected to determine convergence. These points are skin probes S-25, S-35, S-45, S-31, S-32, and S-33. Additional probes on the rib and longeron, not visually depicted on the demonstrator panel, were also evaluated.

The total displacement of the probe sensors each asymptotically approach a converged value as the number of elements in the structural mesh increases, as illustrated in Fig. 9. The displacement error, along with the computational cost in wall clock time, are provided in Fig. 10. The displacement change converges between the 50,000- and 140,000-element meshes. The cost trend for increasing the number of mesh elements is approximately linear, so higher spatial fidelity analyses are feasible if desired. This linear forecast is limited by the system memory available, as the largest mesh evaluated required close to the computer available 128 GB memory.

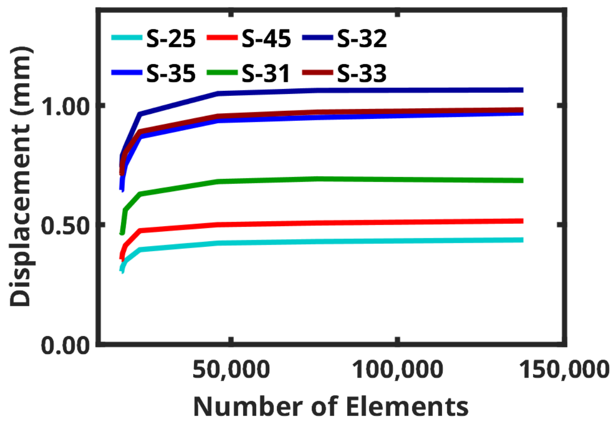

Figure 9: Displacement of finite element convergence probes on the demonstrator panel with a steady 890 N (200 lbf) load for a subset of locations assessed.

Using these results, the mesh with approximately 76,000 elements was selected for the remainder of this study (Fig. 11), as it exhibits a maximum displacement error of less than 2% for all probe points and provides a good balance of compute performance. This corresponds to a global mesh size parameter of 0.0075. For all component panels, the mesh contains at least two elements across the most narrow features, as illustrated for some narrow elements, such as longerons in Fig. 11b.

4.2. Temporal Convergence

For analysis with dynamic loads, unsteady simulations also require an assessment of the time fidelity of the analysis to determine the appropriate time steps. Sufficiently small time steps are required to fully capture the response of the panel to dynamic loading. For

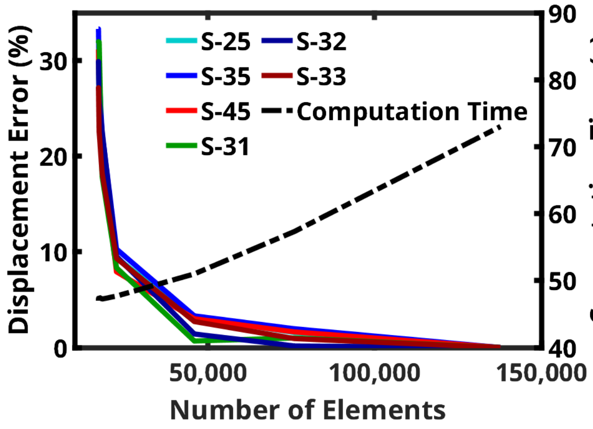

Figure 10: Error and computational cost of finite element convergence probes on the demonstrator panel with a steady 890 N (200 lbf) load for a subset of locations assessed.

the temporal convergence study, a sinusoidal loading was prescribed, and the response in the laminate out-of-plane Z-displacement, was evaluated for time steps varying between 20 to about 400 time-steps-per-cycle of loading. The sinusoidal loading was a transverse pressure applied uniformly to the panel at a frequency of 8.84 Hz and with a magnitude of 34.5 kPa (5 psi). Similar to the mesh convergence study, the convergence criteria used was a percent error of the local displacement for each probe, using the highest temporal resolution as the true value.

Figure 12 exemplifies the observed displacement response of the S-45 probe for a duration of five loading cycles. The lowest-resolution solution with 20 steps/cycle clearly fails to capture the finer motions of the response. The next-lowest solution, with 40 steps/cycle, does capture the primary motions of the response, but with some error in magnitude and phase with respect to the highest-resolution solutions. At 80 steps/cycle and higher, the differences are more difficult to visually observe.

The accuracy of each response to a transient load is more visually apparent when frequency-domain solutions were compared. For example, single-sided amplitude and phase spectra are shown in Fig. 13, with the loading frequency and phase plotted for reference. These errors at the loading frequency only are compared, along with simulation cost, in Fig. 14. At 80 steps/cycle, the amplitude and phase each have approximately a 2% error, which are minimized to <0.5% at the 200 steps/cycle. A time step size of approximately 100 steps/cycle is likely sufficient.

4.3. Experimental Validation

With the mesh defined, the static loading can be compared to the UofSC static test results described ear-

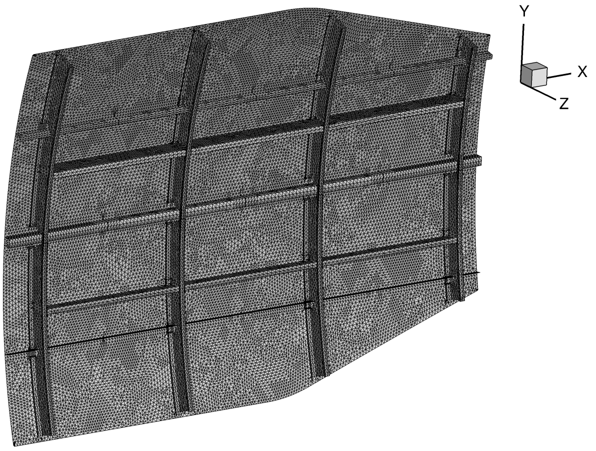

(a) Mesh overview.

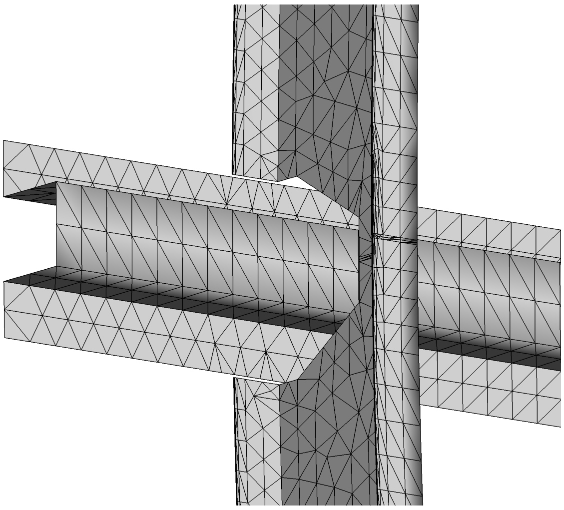

(b) Mesh detail on demonstrator frame elements.

Figure 11: Demonstrator panel mesh comprised of approximately 75,000 elements.

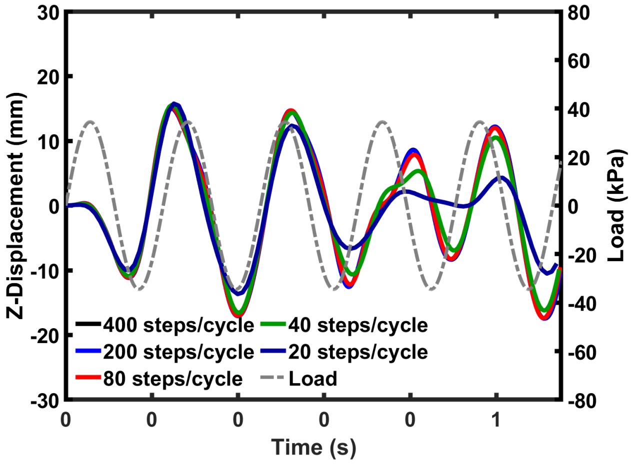

Figure 12: Finite element time history of Z-displacement at S-45 probe for the demonstrator panel with prescribed sinusoidal loading.

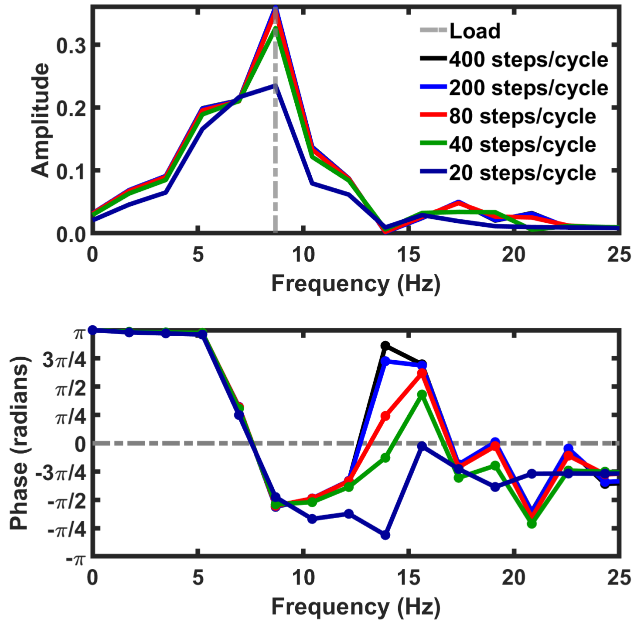

Figure 13: Single-sided amplitude and phase content of Z-displacement at S-45 probe for the demonstrator panel with prescribed sinusoidal loading.

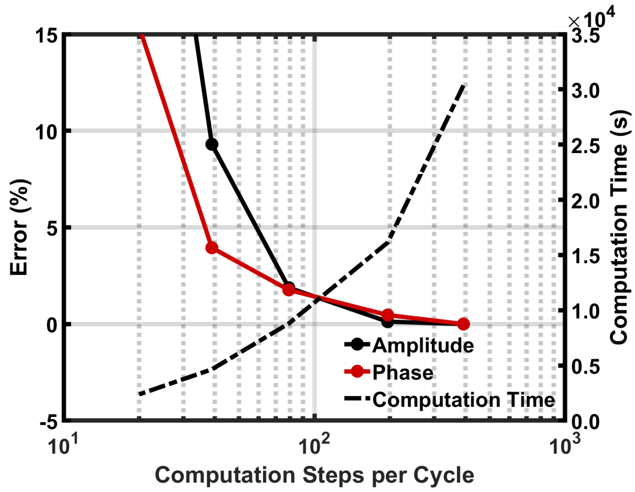

Figure 14: Example error at the S-45 probe Z-displacement at loading frequency, and computational cost of analysis for demonstrator panel with prescribed sinusoidal loading.

lier.

The computational analysis applied pinned-roller boundary conditions supporting the panel, similar to a bridge truss analysis. The load is added as a force acting over a wide area, mimicking the load area of the rubber pads in the experiments. The pristine panel was evaluated for both the moderate and high loads. For all "Damage" cases, the moderate 356 N (80 lbs) load was applied and then increased to the high load of 667 N (150 lbs). The damage was applied at the locations noted in Fig. 15. The experimental results are the mean of the measurements over the loading time. The uncertainly is within approximately 1-10 $\mu\varepsilon$.

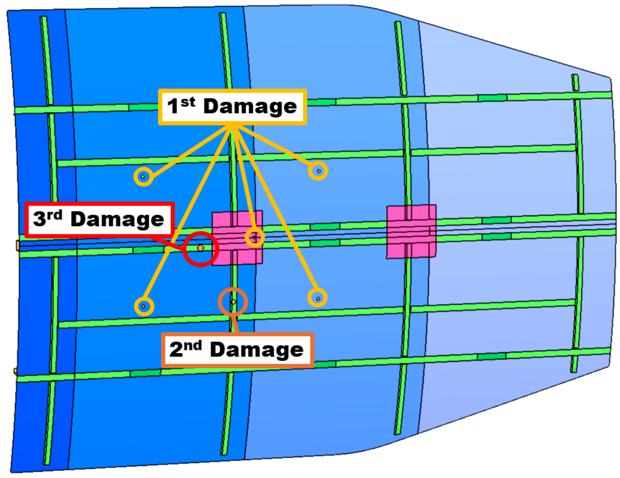

Figure 15: Locations of impact damage on demonstrator panel model.

The validation occurred after multiple damage tests:

- No Damage: The panel loaded with zero damage
- 1st Damage: The panel loaded after 5 $\times$ 14.56 J impacts
- 2nd Damage: The panel loaded after an additional 36.59 J impact
- 3rd Damage: The panel loaded after a further additional 61.00 J impact

Overall, the computational predictions are closer for the G-X1 sensor than the G-Y1 sensor. The sensor strains are presented in Fig. 16. These differences are attributed to the ply directionality and the physical area between the structural members. The skin in the x-direction has a significant distance without a structural member, whereas the sensor in the y-direction has only a small skin area between the members.

The differences in delta strain and percent errors are provided in Table 3. No matter the load level, or whether the panel is pristine or damaged, the strain prediction for sensor G-X1 is within 6 $\mu\varepsilon$ compared to the experimental measurement, and usually well below 5 $\mu\varepsilon$. Conversely, the the strain prediction for sensor G-Y1 tends to be larger, up to about 33 $\mu\varepsilon$, though usually within 15 $\mu\varepsilon$. The percentage errors are presented, but can be misleading for values near zero, where the values are significantly larger than the delta strain implies.

Interestingly, the strain measurements from the experiment show little to only small changes after damage. The extent of the damage for the computational approach was obtained from thermographic analysis at the ULI partner at NCAT (21, 22), as the current analysis does not model impacts. The irregular damage regions were estimated by circular representa-

Table 3: Comparison of the Measured and Predicted Numerical Strain Differences under Static Loading with and without Impact Damage.

	356 N (80 lbs)		667.2 N (150 lbs)	
	G-X1	G-Y1	G-X1	G-Y1
	Δ (%)	Δ (%)	Δ (%)	Δ (%)
Pristine	-6.1 (24%)	-2.0 (-9%)	4.4 (11%)	10.4 (-30%)
Damaged				
1st	0.2 (-1%)	-27.4 (-979%)	3.1 (8%)	32.7 (-246%)
2nd	2.9 (-17%)	-7.5 (-44%)	1.2 (3%)	11.4 (-33%)
3rd	0.02 (-0.1%)	-12.2 (-99%)	3.4 (8%)	14.4 (-46%)

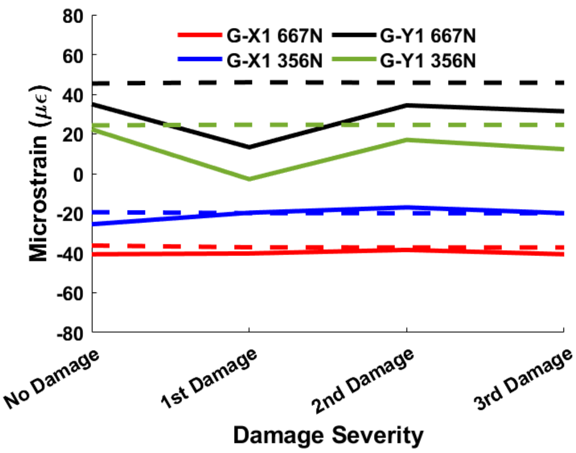

Figure 16: Experimental (solid) and computational (dashed) strain on the demonstrator panel.

Table 4: Modelled Dimensions of Impact Damage for all Damage Events.

Damage Event	Damage Radius (mm)	Number of Plies Removed
1st (upper-left)	4.75	7
1st (upper-right)	5.26	10
1st (center)	8.72	9
1st (lower-left)	4.87	9
1st (lower-right)	5.13	9
2nd	9.11	9
3rd	12.19	7

tions whose material definitions excluded the damaged plies that from the top of the laminate stack. The estimated damage for each event is enumerated in Table 4. As the trends are similar, and the differences are relatively small, the damage estimates are considered to be sufficiently realistic. The differences in the estimated and actual damage areas/depths could be the origin of these differences, in particular for the y-direction strains. In addition, after the first damage event, subsequent damage occurs on or adjacent to structural elements, which can minimize the effects of the panel failure.

5. RESULTS

The remainder of this work focuses exploring two aspects of the demonstrator panel. First are the sensitivities of the outcomes for integrated panels (influence of boundary conditions) and details of the thermoplastic layup (material properties). Second are specific applications of the notional demonstrator panel for AAM, specifically illustration of the effects of impact damage and behavior in rotor wake conditions.

5.1. Panel Sensitivity Analysis

5.1.1. Influence of Boundary Conditions

The demonstrator panel is a single representative panel. In an AAM vehicle, it would be part of a number of panels attached to one another via boundary conditions. To develop an understanding of the sensitivity of the demonstrator to these potential boundary conditions, four sets of boundary conditions were studied under a prescribed sinusoidal load. The boundary conditions were selected to be representative of the notional panel as a component in a larger structure. The boundaries, depicted in Figure 17, are the edges of the panel aerodynamic skin surface and the edges of the ends of the structural frame. The skin edges are defined as either clamped (zero displacement, zero rotation) or pinned (zero displacement, free rotation). The frame edges are defined as either fixed (zero displacement, zero rotation) or free (free displacement, free rotation). For this comparison, four sets of boundary conditions were numerically evaluated: clamped-fixed, clamped-free, pinned-fixed, and pinned-free.

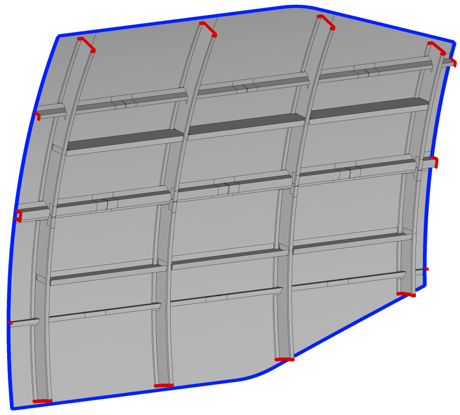

Figure 17: Boundary condition groups: skin boundary (blue) and frame boundary (red).

The loading conditions for these trials were a prescribed uniform sinusoidal load with an amplitude of 44.5 N (10 lbs) and frequency of 8.84 Hz. The pressure across the panel is dependent on mesh spacing and represents and average pressure of 34.5 kPa (5 psi). This value was selected to elucidate differences in selected test cases which represent an upper bound on maximum loading conditions of high speed forward flight with the addition of non-linear gusts or strong rotor downwash. This upper bound also provides exemplar structural failures. The frequency of the sinusoidal gust was selected as it correlates to the 1 per rev frequency of the NASA quadrotor, thus showing a fully reversed loading condition on a time scale appropriate for AAM vehicles.

One of the goals of the OAT analysis is an assessment of when maintenance and/or repair is needed. This can be assessed by material residual strength, particularly after damage, or the Kreisselmeier–Steinhauser (K-S) index. Using TACS, the sensitivity of these panels with different boundary conditions was assessed with the continuous K-S failure index (20). The K-S failure value is based on the strain (ε_m) that produces the maximum failure criterion within the computational domain. A value of one or higher indicates that failure of the structure at the location of interest has occurred.

For the sinusoidal loading, the K-S failure values are provided in Fig. 18 for both the mean and maximum loading values. While in general the mean and maximum trends are similar, they are not always identical. When the skin is pinned rather than clamped, the potential for failure is higher, as evidenced by the higher means and maximums, some which indicate failure under these conditions (maximum value exceeds one). As expected, when the supporting structure is clamped, the potential is higher for failure than when the structure has additional flexibility (free condition). It is also clear that the skin thickness (thickness decreases as sensor number increases) has a significant impact on the K-S failure prediction with dynamic loading.

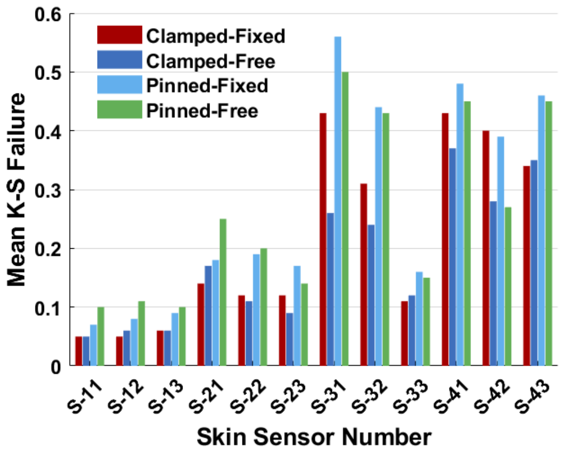

(a) Mean

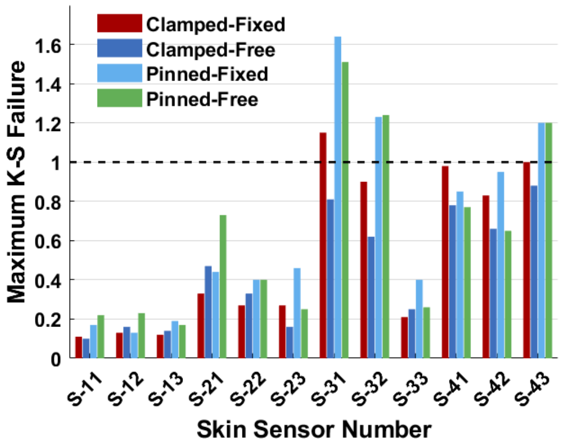

(b) Maximum

Figure 18: Variation in K-S failure index predictions with panel boundary conditions.

5.1.2. Influence of Structural Material Definition

The importance of detailed material layouts of the thermoplastic has been evaluated. While the vehicle or composites manufacturer will have these details, they will be proprietary and not shared. While the OAT is being constructed to protect these data for use in evaluations, it may be that these details will not be available. Therefore, an assessment of simplifications that may be the only data available to the operator have been assessed.

Three levels of fidelity in the material property on the panel have been assessed:

- Lamina: the most accurate, uses ply-by-ply material definitions for all components. Each component has a defined reference direction, as well as an angle and thickness for every ply in the stack.
- Laminate: equivalent elastic properties for the entire stack have been determined. The inputs are the reference direction, orthotropic material properties and thickness of the entire laminate.
- Isotropic: The laminate stack is balanced and symmetric forming a quasi-isotropic membrane. The only inputs are isotropic elastic properties and the thickness of the laminate, without any directionality.

The equivalent elastic material properties of the laminate stack were calculated using methods from Nettles (23) and Chou et al. (24).

Test conditions applied here are the same sinusoidal loading applied in the Temporal Convergence section, with pinned-fixed boundary conditions applied on the panel. The sensitivities to the material have been evaluated with the K-S failure index, as previously discussed. The mean and maximum K-S failure values are presented for each skin sensor evaluated in Fig. 19. For the laminate estimate, the K-S mean and maximum values, with the exception of the S-11 sensor mean, are 150% or higher than the lamina (nominally exact) values. While there are significant differences between the two, the laminate estimate proves to be very conservative. The extent of the conservative prediction for the maximum K-S failure value is dependent primarily on the skin thickness. There is not a linear correlation of the skin thickness with the over prediction of the K-S failure value. However, this trend does indicate that if detailed layout data are not available, that a lamina estimate is usable for tracking damage.

If no data are available for the thermoplastic material beyond the skin thickness, then an isotropic analysis is the option available. Evaluating again the mean and maximum K-S failure index predictions for each skin sensor in Fig. 19, the isotropic assumption provides overall more accurate predictions than the laminate estimation, except for the sensors near the panel edges. For all sensors, the potential for failure is under predicted, so that the use of these data will not be conservative. Thus, if an isotropic assumption is necessary, a safety factor of 100% or higher will likely be necessary for internal locations, with additional factors of safety near the panel edges. As skin thickness decreases there is a strong quadratic relationship for the accuracy of the K-S failure index between the lamina and laminate assumptions, trending towards linear as the location of the sensor moves toward the edge of the panel. The isotropic assumption formed a strong inverse linear relationship with thickness compared to the exact layup predictions, with accuracy decreasing as the sensor location moves towards the panel edges. These again may be strongly dependent on the actual layup of the material.

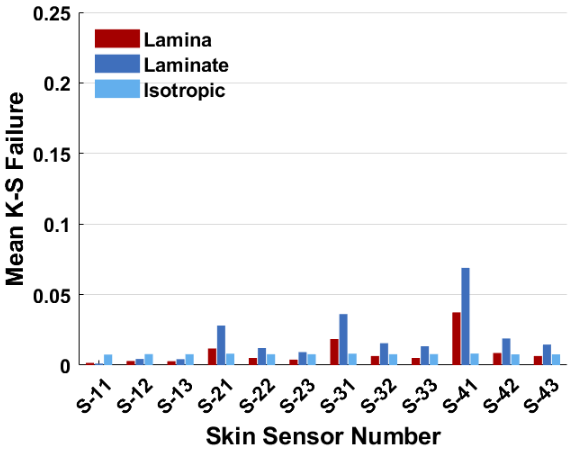

(a) Mean

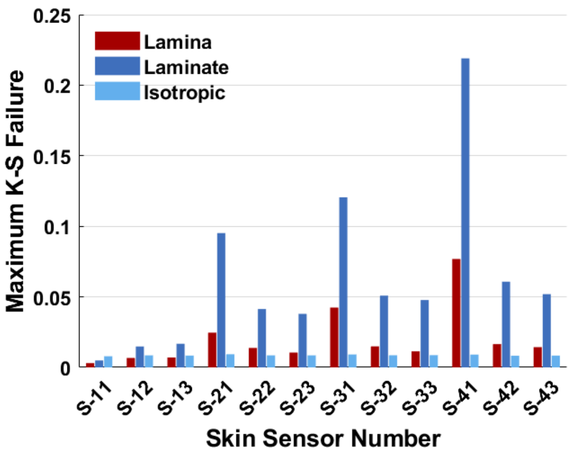

(b) Maximum

Figure 19: Variation in K-S failure index predictions with panel material properties.

It is important to clarify details of the use of the K-S failure index in the context of the material properties. The laminate approximation to the exact structural layup (lamina) appears to be less accurate than the more general isotropic assumption. The directional strains predicted by the laminate are more accurate than the isotropic assumption, as illustrated in Fig. 20. As the K-S failure value, defined previously in Eqn. 1, is an aggregate, the principal direction of failure may be independent of the orthotropic ply directions, and it is highly dependent on the ply layout of the thermoplastic (or any composite) material. In this particular demonstrator panel, the K-S failure value for the laminate is significantly different, but this may not be the case for other layouts. Overall, the K-S prediction for laminate assumptions does tend to be conservative compared to the exact layout.

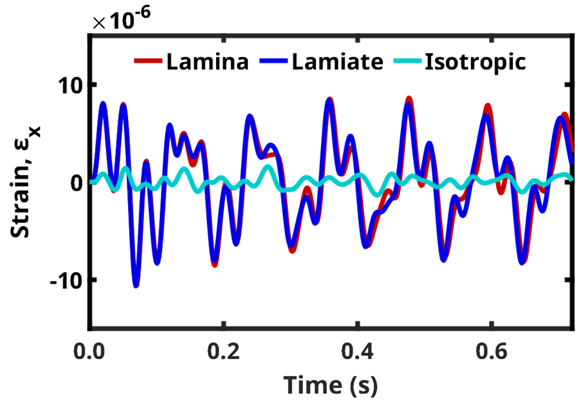

(a) Longitudinal strain time history at S-32 probe.

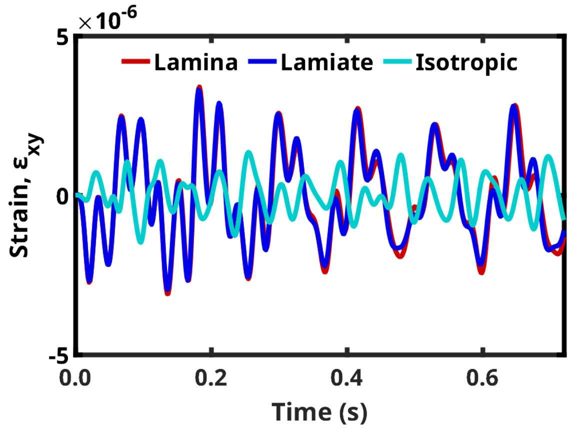

(b) Shear strain time history at S-32 probe.

Figure 20: Comparison of the predicted strains applying different panel material properties.

5.2. Effects of High-Frequency Rotor Airloads

Using the dynamic airloads described earlier, the influence of the rotor airloads was assessed for the advance ratio of 0.15 at a location forward of the fuselage (red location in Fig. 3). The nominal thrust coefficient (C_T) applied in this analysis, 0.0064, is representative of a quadrotor type configuration in cruise at an approximate weight of 1815 kg (4000 lbs).

It is clear from the K-S mean and maximum failure values in Fig. 21. The 5-bladed rotor at lower tip speed has the least impact on the potential for failure, typically less than half of the value for the other conditions for both the mean and maximum values.

5.3. Effects of Impact Damage

It is anticipated that AAMs will experience higher damage risks to composite panels due to impact events which may or may not be known to the operator. These impacts may cause permanent structural damage, which change the load paths and strain field of the panel. Prior work (21, 22) has performed impact testing with thermographic evaluation on the demon-

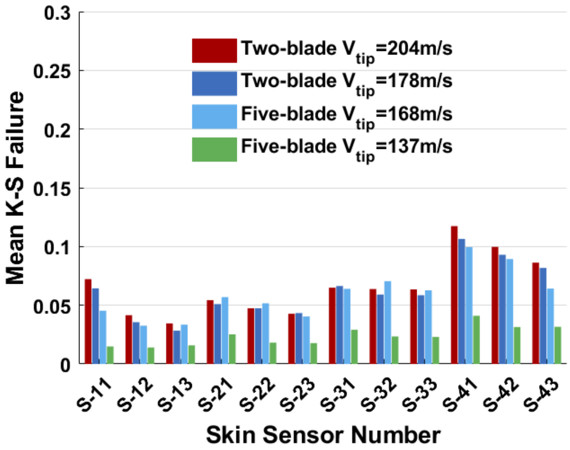

(a) Mean

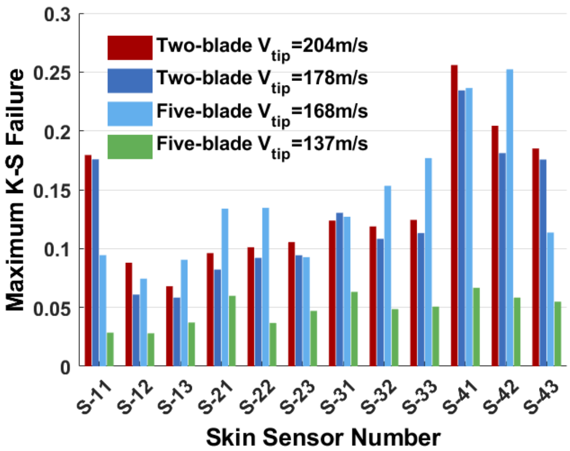

(b) Maximum

Figure 21: Variation in K-S failure index predictions with rotor downwash.

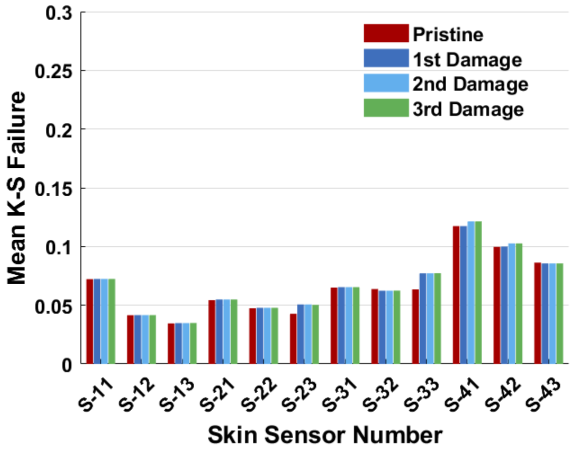

(a) Mean

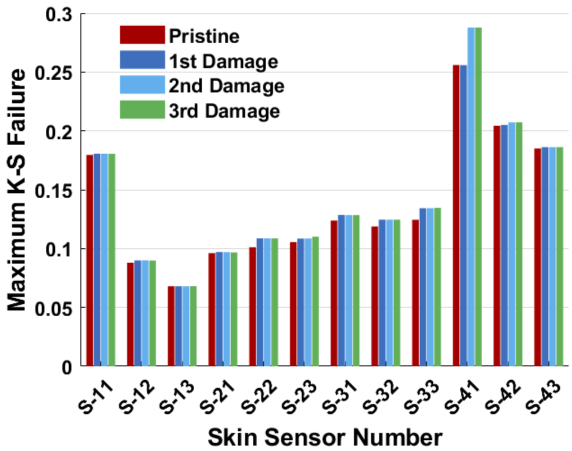

(b) Maximum

Figure 22: Variation in K-S failure index predictions with rotor downwash on damaged panel.

strator panel and on test coupons to quantify the damage on the composite layup that an impact event of a known energy incurs.

To bound the scope that effects of non-catastrophic damage on prediction of K-S-based failure for this composite material, three levels of damage at locations were applied. These damage locations and sizes mimic prior experimental work performed by partner universities. The damage to the composite at each impact site was applied by assuming the damage caused a circular region of damage, where the composite plies with any damage are removed and contribute zero stiffness to the material, as in the Experimental Validation section and Table 4. The assessment shown herein applied the rotor downwash conditions of the 2-bladed rotor with a V_{tip}= 204 m/s, so that comparisons can be established.

As with the prior assessments, the objective is to assess the potential failure of the panel, so that again the mean and maximum K-S predicted failure value was evaluated, as visualized in Fig. 22. The effect of different impact damage events (Table 4 and Fig. 15) was assessed at the different sensors. Overall, the additional, the damage did not significantly change the prediction of failure compared to the pristine panel at most of the sensors. Only the sensor located near the panel edge with the thinnest skin deviated more than 10% as additional damage was added to the panel. This behavior can be partially attributed to the fact that the locations of the damage applied after the first damage location were close to structural elements, such as ribs and spars (Fig. 15). This is clearly observed in Fig. 24 where the high values of K-S failure after the third damage event are concentrated near damage event one where there were no structural supports. Additional higher K-S failure values are found near the panel edges and for the thinnest skin. The first damage, applied to panel areas where the skin is not supported, shows that the K-S failure values

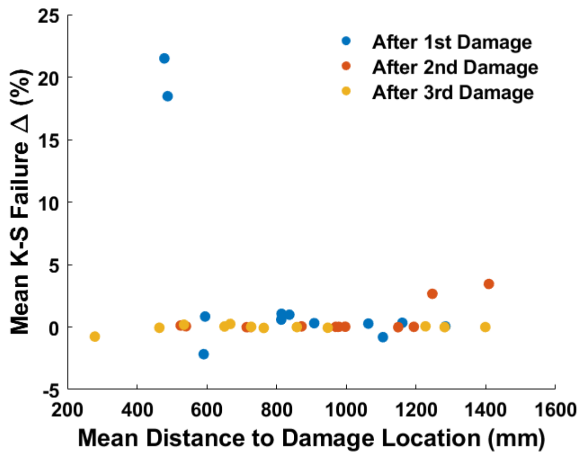

(a) Mean

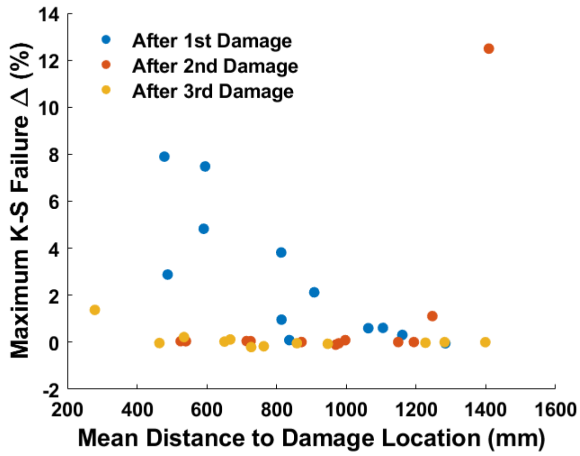

(b) Maximum

Figure 23: Difference in K-S failure index prediction with mean sensor distance from damage location.

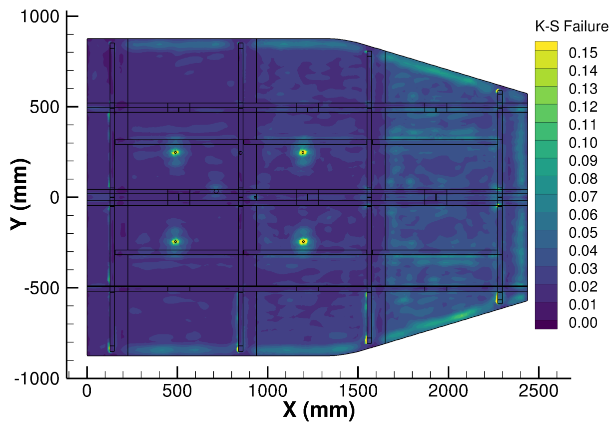

(a) Full panel

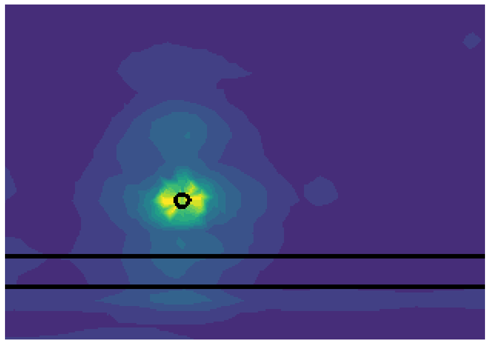

(b) Local field near a damage 1 site

Figure 24: K-S failure index field across the demonstrator panel after 3rd damage event.

rapidly decrease to a mean value away from that location (Fig. 24b)), but the effects of the damage are observed throughout the panel. Thus, additional skin damage to the panel may result in increased potential for failure.

One of the objectives of another portion of this ULI is the incorporation of sensors during flight to monitor the damage. To minimum weight and cost, optimal sensor numbers and placement are being sought (Ref. (25)). Figure 23 examines this relationship for the demonstrator and damage events. As expected, the highest potential of failure occurs between the pristine and first damage events. A general linear trend between the damage site and location of the sensors is observed for the maximum K-S failure, but the mean exhibits no clear trend. The damage between subsequent events is relatively negligible, as previously observed in Fig. 22. Figure 23 does illustrate that the thinner skin, even while farthest from the damage site in most instances, exhibits a higher sensitivity to potential failure.

6. CONCLUSIONS

As part of a research effort to address the individual needs of Advanced Air Mobility (AAM) vehicles, exploration of the requirements for structural behavior of an advanced thermoplastic composite have been explored. From the subset effort presented in this paper, the following conclusions may be drawn:

- The TACS methodology can provide accurate prediction of structural behavior of AAM thermoplastic panels.
- The influence of the boundary conditions on strain and the potential of failure are overall not strongly correlated with thermoplastic skin thickness.
- While the laminate estimate of the thermoplastic skin panel K-S failure value behavior can be significantly different to its exact lamina behavior, depending on the direction of failure, the data are conservative. Prediction of the strain indicate that the numerical approach is sound. The errors in the predicted failure increase as skin thickness decreases.
- Isotropic material estimates may yield closer estimates of the K-S failure behavior than laminate for locations away from the edges of the panel.

These K-S failure index estimates are consistently under predicted, so that the use of isotropic estimates will need a safety factor and be limited to central panel locations.

- The estimated K-S failure value is relatively comparable across the panel skin location for blade number and tip speed. The least potential for damage is higher number of blades at lower speeds.
- The thermoplastic panel was subjected to moderate damage at subsequent, multiple locations. The prediction of the K-S failure value behavior was relatively constant as additional damage was applied when there were structural support members near the damage location. The most change in failure potential was observed for the thinnest skin near the panel edge.

7. ACKNOWLEDGMENTS

This effort is partially funded by the NASA University Leadership Initiative (ULI), *Innovative Manufacturing, Operation, and Certification of Advanced Structures for Civil Vertical Lift Vehicles (IMOCAS)*, Cooperative Agreement 80NSSC21M0113. Mia Siochi is the NASA technical monitor.

The authors would like to thank, as part of the NASA ULI, Abdel Bayoumi at the University of South Carolina and Mannur Sundaresan of North Carolina A & T for use of the pristine and damaged data for the demonstrator panel, and Ian Derx of Qarbon Aerospace for the construction and details of the demonstrator panel.

The authors would also like to thank the many students who have contributed to the development of the TACS/ESP approach, in particular Sean Engelstad and Brian Burke.

The views and conclusions contained in this document are those of the authors and should not be interpreted as representing the official policies of position, either expressed or implied, of the National Aeronautics and Space Administration (NASA) or the U.S. Government.

8. REFERENCES

[1] Silva, C., Johnson, W. R., Solis, E., Patterson, M. D., and Antcliff, K. R., "VTOL Urban Air Mobility Concept Vehicles for Technology Development," 2018 Aviation Technology, Integration, and Operations Conference, Atlanta GA, June 2018. DOI: 10.2514/6.2018-3847

[2] Kopardekar, P., "Transformative Vertical Flight 2020 Panel, NASA Perspective," Proceedings of the 2020 VFS Transformative Vertical Flight Conference, San Jose, CA, January 21–23 2020.

[3] Crown Consulting, Ascension Global, Georgia Tech, and McKinsey and Co., "Urban Air Mobility Market Study," https://www.nasa.gov/sites/default/files/atoms/files/uam-market-study-executive-summary-v2.pdf, November 2018.

[4] Piringer, M., Grimmond, C. S. B., Joffre, M. P., S. M., Middleton, D. R., Rotach, M. W., Baklanov, A., De Ridder, K., Ferreira, J., Guilloteau, E., Karppinen, A., Martilli, A., Masson, V., and Tombrou, M., "Investigating the Surface Energy Balance in Urban Areas – Recent Advances and Future Needs," *Water, Air and Soil Pollution: Focus*, Vol. 2, 2002, pp. 1–16. DOI: 10.1023/A:1021302824331

[5] Barlow, J. F., "Progress in observing and modelling the urban boundary layer," *Urban Climate*, Vol. 10, ICUC8: The 8th International Conference on Urban Climate and the 10th Symposium on the Urban Environment, 2014, pp. 216–240. DOI: https://doi.org/10.1016/j.uclim.2014.03.011

[6] Stull, R., *Practical Meteorology: An Algebra-based Survey of Atmospheric Science -version 1.02b*, Dept. of Earth, Ocean Atmospheric Sciences, University of British Columbia, 2017.

[7] Smith, M. J., Crawford, A., and Carozza, K., "Development of an Operational Analysis Tool for Urban Air Mobility," Proceedings of the 79th Vertical Flight Society Annual Forum, May 16–18 2023. DOI: 10.4050/F-0079-2023-18135

[8] Kennedy, G. J., and Martins, J. R., "A parallel finite-element framework for large-scale gradient-based design optimization of high-performance structures," *Finite Elements in Analysis and Design*, Vol. 87, 2014, pp. 56–73. DOI: https://doi.org/10.1016/j.finel.2014.04.011

[9] Boopathy, K., and Kennedy, G. J., "Parallel Finite Element Framework for Rotorcraft Multibody Dynamics and Discrete Adjoint Sensitivities," *AIAA Journal*, Vol. 57, (8), 2019, pp. 3159–3172. DOI: 10.2514/1.J056585

[10] Bathe, K.-J., and Dvorkin, E. N., "A formulation of general shell elements—–the use of mixed interpolation of tensorial components," *International Journal for Numerical Methods in Engineering*, Vol. 22, (3), 1986, pp. 697–722. DOI: 10.1002/nme.1620220312

[11] Haimes, R., and Dannenhoffer, J., "The Engineering Sketch Pad: A Solid-Modeling,

Feature-Based, Web-Enabled System for Building Parametric Geometry," 21st AIAA Computational Fluid Dynamics Conference, 2013. DOI: 10.2514/6.2013-3073

[12] Dannenhoffer, J., "OpenCSM: An Open-Source Constructive Solid Modeler for MDAO," 21st AIAA Fluid Dynamic Confer- ence, 2013. DOI: 10.2514/6.2013-701

[13] Smith, M. J., Shenoy, R., Kenyon, A. R., and Brown, R. E., "Vorticity-Transport and Unstructured RANS Investigation of Rotor-Fuselage Interactions," Proceedings of the 35th European Rotorcraft Forum, September 22–25 2009.

[14] J. Taylor and K. Munson, editors, *Jane's All the World's Aircraft*, Jane's Publishing Company, 1986-1987.

[15] Pascioni, K. A., Thai, A. D., and Bain, J. J., "Propeller Source Noise Separation from Flight Test Measurements of the Joby Aviation Aircraft," 30th AIAA/CEAS Aeroacoustics Conference (2024), 2024. DOI: 10.2514/6.2024-3231

[16] Whiteside, S., Pollard, B., Antcliff, K., Zawodny, N., Fei, X., Silva, C., and Medina, G., "Design of a Tiltwing Concept Vehicle for Urban Air Mobility," Technical Report TM–20210017971, NASA, 06 2021.

[17] Thai, A. D., *Development of high-fidelity computational methods for prediction of multirotor aerodynamics, aeroacoustics, and trim*, Ph.D. thesis, Boston University, 2022.

[18] Qarbon Aerospace, "Qarbon Aerospace," https://qarbonaerospace.com, [Online; accessed 7-August-2024], 2021.

[19] Wrenn, G. A., "An indirect method for numerical optimization using the Kreisselmeir-Steinhauser function," Technical report, NASA, 1989.

[20] Kennedy, G. J., and Hicken, J. E., "Improved Constraint-Aggregation Methods," *Computational Methods in Applied Mechanical Engineering*, Vol. 289, 2015, pp. 332–354. DOI: 10.1016/j.cma.2015.02.017

[21] Travis Obie-Rolle, Manoj Rijal, and Mannur Sundaresan, "Monitoring Damage Development in Carbon/Thermoplastic Composite Materials," Presented in Acoustic Emission Working Group: 64th Annual Conference, 2023.

[22] Dhar, P. and Rijal, M. and Sundaresan, M.J., "Poster: Assessing Impact Damage in Carbon/Thermoplastic Composites using Active Flash Thermography," Presented at the American Society of Nondestructive Testing 32nd Research Symposium, 2024.

[23] Nettles, A. T., "Basic Mechanics of Laminated Composite Plates," Technical Report NASA-RP-1351, NASA, 10 1994.

[24] Chou, P., Carleone, J., and Hsu, C., "Elastic Constants of Layered Media," *Journal of Composite Materials*, Vol. 6, (1), 1972, pp. 80–93. DOI: 10.1177/002199837200600107

[25] Li, Ai and Dickson, Samuel and Henderson, Bryson and Ziehl, Paul and Houck, Sydney, "Identifying the Energy of Low-velocity Impacts on Composite Components Using Acoustic Emission," Presented at the IEEE Aerospace Conference, Big Sky, MT, 2023. DOI: 10.1109/AERO55745.2023.10116008